



Incipient ferroelectricity and conductivity relaxations in $\text{Dy}_2\text{Ti}_2\text{O}_7$



N. Zhang^a, H. Wang^a, Y.D. Li^a, Q.J. Li^a, S.G. Huang^a, Y. Yu^a, J. Zheng^b, C. Cheng^b, C.C. Wang^{a,*}

^a Laboratory of Dielectric Functional Materials, School of Physics & Material Science, Anhui University, Hefei 230601, PR China

^b Center of Modern Experimental Technology, Anhui University, Hefei 230039, PR China

ARTICLE INFO

Article history:

Received 16 November 2015

Received in revised form

20 April 2016

Accepted 21 April 2016

Available online 25 April 2016

Keywords:

Dielectric property

Electric modulus

Incipient ferroelectricity

Conduction relaxations

ABSTRACT

$\text{Dy}_2\text{Ti}_2\text{O}_7$ ceramic samples were prepared via the solid-state reaction route. The dielectric properties of the sample were systematically investigated in the temperature range from 4 K to 973 K and the frequency range of 100 Hz to 1 MHz. Both Raman and low-temperature (down to 4 K) dielectric measurements indicate incipient ferroelectricity in the $\text{Dy}_2\text{Ti}_2\text{O}_7$ sample. In addition, two relaxations were observed in the temperature range above 450 K. Our results indicate that the two relaxations are related to conductivity relaxation associated with singly and doubly ionized oxygen vacancies.

© 2016 Elsevier B.V. All rights reserved.

1. Introduction

Multiferroic materials, in which magnetic and electric orders coexist, have recently become the focus of much research because of their unusual physics and potential applications [1–4]. Among the presently-known multiferroic materials, a family of rare-earth titanates ($\text{R}_2\text{Ti}_2\text{O}_7$) has attracted a great deal of interest in recent years because of its interesting dielectric, piezoelectric, and ferroelectric properties [5–7]. $\text{R}_2\text{Ti}_2\text{O}_7$ compounds usually crystallize with a cubic pyrochlore type structure [8–11] for ions with smaller radii (e.g., $\text{R}^{3+} = \text{Sm}^{3+} - \text{Lu}^{3+}$) or a monoclinic structure for ions with larger radii (e.g., $\text{R}^{3+} = \text{La}^{3+} - \text{Nd}^{3+}$) [6,12] and some of them are ferroelectrics with very high Curie points [13]. In recent years, $\text{R}_2\text{Ti}_2\text{O}_7$ compounds with a pyrochlore type structure [14–17], especially $\text{Dy}_2\text{Ti}_2\text{O}_7$ (DTO) [18–20], have attracted much attention because of their spin-ice behaviour and large low-temperature paramagnetic magnetic moments.

From the application point of view, dielectric properties are one of the most important properties for multiferroic materials. Unfortunately, the investigation of the dielectric properties of DTO is incomplete. Saito et al. reported the magneto dielectric response of single crystals of $\text{Dy}_2\text{Ti}_2\text{O}_7$ down to 0.26 K [18]. Belov et al. reported the dielectric properties of Ca-doped $\text{Dy}_2\text{Ti}_2\text{O}_7$ ceramics in the low-

frequency range (0.5–500 Hz) [21]. The nature of the dielectric properties of DTO has not yet been fully characterized.

We, herein, presented detailed investigations on the dielectric properties of DTO ceramics over wide temperature (4–973 K) and frequency (100 Hz–1 MHz) ranges. Incipient ferroelectricity was confirmed in the sample. Two relaxations were observed, and their mechanisms were discussed.

2. Experimental

Single-phase DTO ceramic samples were prepared by the solid-state reaction method using high-purity (99.99%) starting powders of Dy_2O_3 and TiO_2 . First, the powders of Dy_2O_3 were calcined at 900 °C for 10 h in air to dehydrate. Then, stoichiometric powders (1:2) of Dy_2O_3 and TiO_2 were thoroughly mixed using a mortar and calcined at 1300 °C for 10 h in air. After that, the obtained mixture was reground and pressed into pellets with a diameter of 12 mm and thickness of 1–2 mm under a pressure of 20 MPa and finally sintered at 1400 °C for 10 h at a heating rate of 3 °C/min followed by furnace cooling. The phase purity of the sintered pellets was characterized by X-ray diffraction (XRD) performed on a MXP18AHF diffractometer (Mac Science Ltd., Yokohama, Japan) with $\text{Cu K}\alpha$ radiation. The morphology and microstructure of the sintered pellets were studied by a field emission scanning electrical microscope (SEM, Model S-4800, Hitachi Co., Tokyo, Japan). The dielectric properties were measured on a Wayne Kerr 6500B

* Corresponding author.

E-mail address: ccwang@ahu.edu.cn (C.C. Wang).

precise impedance analyser (Wayne Kerr Electronic Instrument Co., Shenzhen, China) with the sample mounted in a holder placed inside a PST-2000HL dielectric measuring system (Wuhan Pusite Instrument Co., Wuhan, China, presenting a temperature range from room temperature to 973 K) and a Janis SHI-4ST-1 closed-cycle cryostat (Research Co., Inc., USA, presenting a temperature range from 4 K to room temperature). The amplitude of the ac measuring signal was 100 mV. Electrodes were made by printing platinum paste on both sides of disk-type samples.

3. Results and discussion

Fig. 1 plots the XRD pattern of the as-prepared DTO ceramic sample which was analysed using Jade 6.0 software. The fitting result was shown as a solid line. The result indicates that the sample is single-phase with a cubic pyrochlore structure and a space group of $Fd-3m$. The calculated lattice parameter of $a = 10.0937 \text{ \AA}$ is consistent with most of the data in the literature [22,23]. The inset displays the SEM micrograph of the sintered ceramic. It can be observed that the sample exhibits a distinct grain structure, with an average grain size of approximately 1–2 μm .

The temperature (286–973 K) dependence of the dielectric constant $\epsilon'(T)$ (the real part of the complex permittivity ϵ^*) and dielectric loss tangent $\tan \delta(T)$ ($\tan \delta = \epsilon''/\epsilon'$, where ϵ'' is the imaginary part of the complex permittivity) at various frequencies for the DTO sample are shown in Fig. 2(a) and (b), respectively. At temperatures below $\sim 450 \text{ K}$, $\epsilon'(T)$ exhibit a frequency-independent decline similar to that found in SrTiO_3 , CaTiO_3 , and KTaO_3 [24–26]. This behaviour is a common feature for incipient ferroelectrics, which are characterized by increasing dielectric permittivity upon cooling due to the softening of the lowest-frequency polar optical phonon [27]. The dielectric permittivity of an incipient ferroelectric material can be described by the Barrett equation [28].

$$\epsilon'(T) = C \left(\frac{T_1}{2} \coth \frac{T_1}{2T} - T_0 \right)^{-1} + A \quad (1)$$

where C is a constant, T_0 is the hypothetical Curie temperature, T_1 is the onset temperature of quantum fluctuations, and A is the dielectric constant at the high-frequency limit. Fig. 2(c) presents the fitting to the data recorded at 1 kHz by the Barrett equation. Perfect agreement between the experimental data and the fitting curve were obtained. The fitting yields the parameters of $A = 5.6$,

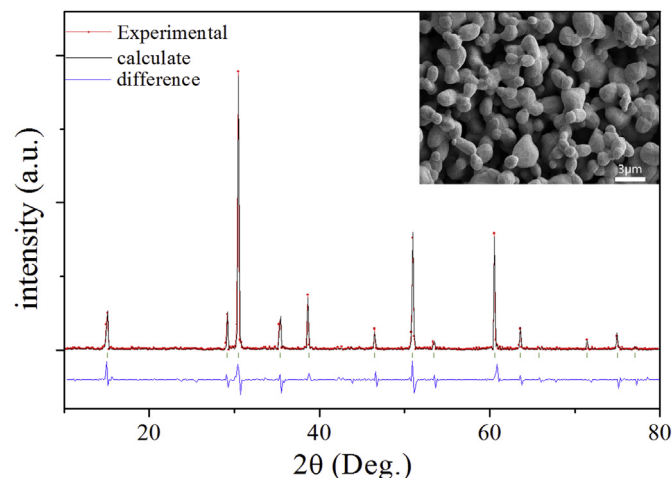


Fig. 1. XRD pattern of the DTO ceramic sample. The inset shows the SEM for an as-prepared pellet of DTO at room temperature.

$C = 56218 \text{ K}$, $T_1 = 0.0046 \text{ K}$, and $T_0 = -1154 \text{ K}$. These values are comparable with those of the titanate oxides of $\text{Ln}_{1/2}\text{Na}_{1/2}\text{TiO}_3$ ($\text{Ln} = \text{La, Pr, Nd, Sm, and Eu}$) [29], indicating the incipient ferroelectric behaviour in the present sample. To further prove this point, we performed dielectric measurements on the DTO pellet in the low-temperature range down to 4 K Fig. 2(d) and (e), present, respectively, the curves of the low-temperature (4–285 K) dielectric constant $\epsilon'(T)$ and the loss tangent of DTO under different frequencies. No peaks were found in the curves of either $\epsilon'(T)$ or $\tan \delta(T)$. The experimental data of the dielectric constant can also be described by the Barrett equation, with the same parameters deduced from the aforementioned fitting. The fitting result of the dielectric constant recorded at 1 kHz was shown as an example in the inset of Fig. 2(c). This finding confirms the incipient ferroelectric nature of the test sample. Very recently, a Raman study on DTO down to 4.5 K also revealed that the modes $F_{2g} \sim 200 \text{ cm}^{-1}$ and $A_{1g} \sim 520 \text{ cm}^{-1}$ linearly decrease with the decreasing temperature [30]. This result further supports the above point.

When the temperature is higher than 450 K, $\epsilon'(T)$ increases rapidly with the increasing temperature. Two stepwise increases occurring at ~ 450 and 700 K can be observed. Correspondingly, two sets of peaks can be identified in the curves of $\tan \delta(T)$, although the second set of peaks can only be observed in the curves recorded under lower frequencies [Fig. 2(b)]. The positions of the peaks shift to higher temperatures with the increasing frequency, indicating that there are two thermally activated relaxations in DTO. For brevity, they were termed as R1 and R2 in the order of ascending temperature. The low-temperature relaxation R1 (above $\sim 450 \text{ K}$) can be well identified in $\tan \delta(T)$, but the high-temperature relaxation R2 (above $\sim 700 \text{ K}$) was obscured in the curves measured with higher frequencies due to the pronounced background. In general, the background in both $\epsilon''(T)$ and $\tan \delta(T)$ is caused by hopping conductivity [31], which obscures the relaxation information. In this case, we apply the electric modulus M^* , which is defined as $M^* = 1/\epsilon^*$. It indicates that the higher the values of ϵ^* caused by the background, the smaller the values of M^* that can be obtained. Therefore, the modulus can greatly lessen the background and become a powerful dielectric function in revealing the background-obscured relaxation [32]. Fig. 2(f) shows the imaginary part of the electric modulus M'' as a function of temperature at several frequencies. We can clearly see that a set of relaxation peaks appears in M'' without remarkable background. Although the low-temperature relaxation can be well identified in M'' , the high-temperature relaxation still can only be identified in the lower-frequency curves (e.g., 100 Hz and 1 kHz) in an enlarged view.

Activation energy analysis is favourable for better understanding the relaxation mechanism. Because the peaks of R1 can be well identified from the curves of $M''(T)$, we first focus on this relaxation. The measuring frequency (f) of R1 was plotted as a function of the reciprocal of the peak temperature (T_p), as shown in Fig. 3. The obtained data for R1 fall perfectly on a straight line in the half-logarithmic presentation, implying that the relaxation follows an Arrhenius law

$$f = f_0 \exp(-E_a/k_B T_p) \quad (2)$$

where f_0 is a pre-exponential factor, E_a is the activation energy, and k_B is the Boltzmann constant. The fitting yields values for E_a and f_0 of 0.92 eV and $6.80 \times 10^{11} \text{ Hz}$, respectively.

To calculate the relaxation parameters of R2, we performed detailed dielectric measurements in the frequency domain. Fig. 4 shows the imaginary part of the dielectric modulus M'' as a function of frequency at a series of temperatures. Although the $M''(f)$ curves show two obvious relaxation peaks, the low-frequency peak behaves as a hump superimposed on the high-frequency M'' peak.

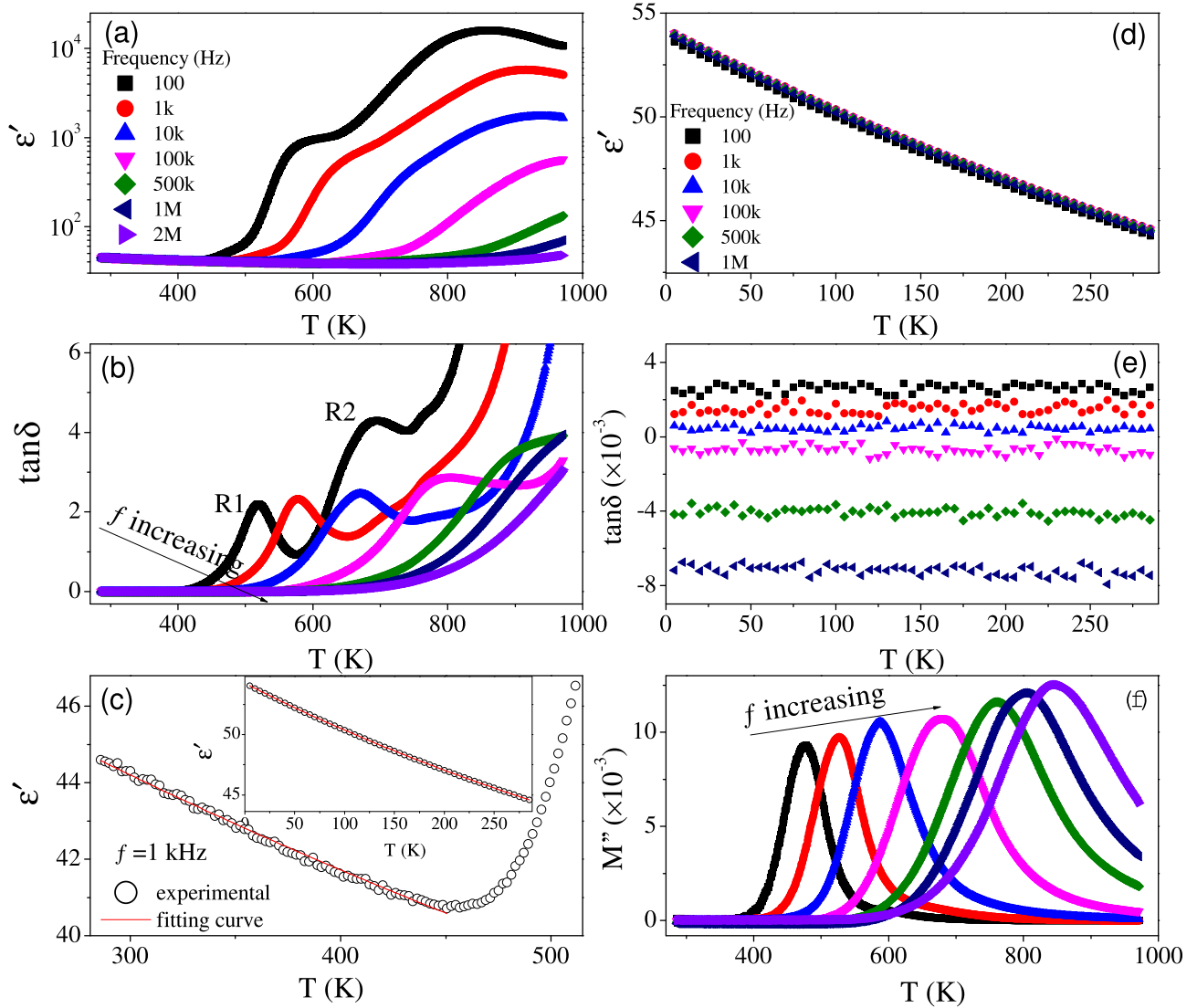


Fig. 2. Temperature dependence of dielectric constant/loss tangent in the high (a)/(b) and low (d)/(e) temperature ranges and the electric modulus (f) for the DTO ceramics. The main panel and the inset of Fig. (c) show the temperature dependence of the dielectric constant recorded at 1 kHz in the high and low-temperature regions, respectively. The solid lines are the fitting curves based on the Barrett equation [Eq. (1)].

For a thermally activated relaxation, the peak position is dominated by the relaxation time (τ). The peak appears at the frequency where $\omega\tau = 1$, and τ generally exponentially decreases with temperature, as described by the Arrhenius relation, the Vogel–Fulcher relation, or a complicated relaxation-time distribution function [33]. As a consequence, the peak moves to a higher temperature (frequency) with the increasing frequency (temperature), and the lower the frequency that appears in the frequency spectrum, the higher the temperature that occurs in the temperature spectrum. Therefore, the low- and high-frequency relaxations correspond to R2 and R1, respectively. To accurately extract the peak position, two Gaussian peaks were used to fit the experimental data. As an example, Fig. 5 displays the comparison between the fitting results and the experimental data measured at 693 K. It is observed that the fitting is perfect. The Arrhenius plots of the two relaxations are displayed in the inset of Fig. 4. Linear fits yield values for the parameters of E_a and f_0 of 0.59 eV and 1.01×10^{12} Hz for low-frequency relaxation and 0.94 eV and 9.78×10^{12} Hz for high-frequency relaxation, respectively. The values for the high-frequency relaxation agree well with those of R1 obtained from the temperature spectra

(Fig. 3.), further confirming that the high-frequency relaxation corresponds to R1. Thus, the low-frequency relaxation can be ascribed to R2.

High-temperature dielectric relaxations in oxides are frequently related to oxygen vacancies. The activation energy of the present relaxations is in the range of 0.3 eV–1.0 eV, which is a typical value for relaxation caused by oxygen vacancies [34–38]. Our recent work showed that, instead of the conventional dielectric relaxation in high-resistivity materials, the relaxation caused by the electromigration of oxygen vacancies at high temperatures is a type of conductivity relaxation [39]. To obtain a deep insight into the physical nature of R1 and R2, we depicted the complex plot of the dielectric permittivity, i.e., the well-known Cole-Cole plot. Fig. 6 shows such plots measured at different temperatures. It is well-known that, for a dielectric relaxation, the Cole-Cole plot should behave as a semicircle for the ideal Debye relaxation or a depressed semicircle for the non-ideal Debye relaxation. The semicircle appears as an n-shaped curve in the double logarithmic representation, as indicated by the curved arrows. The low-frequency terminus of the curve tends to the static dielectric constant (ϵ_s),

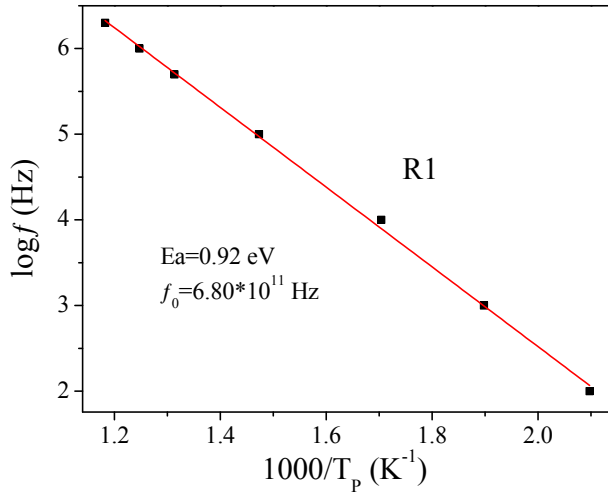


Fig. 3. Arrhenius plot for R1 with the data points obtained from the curves of the electric modulus shown in Fig. 2(d).

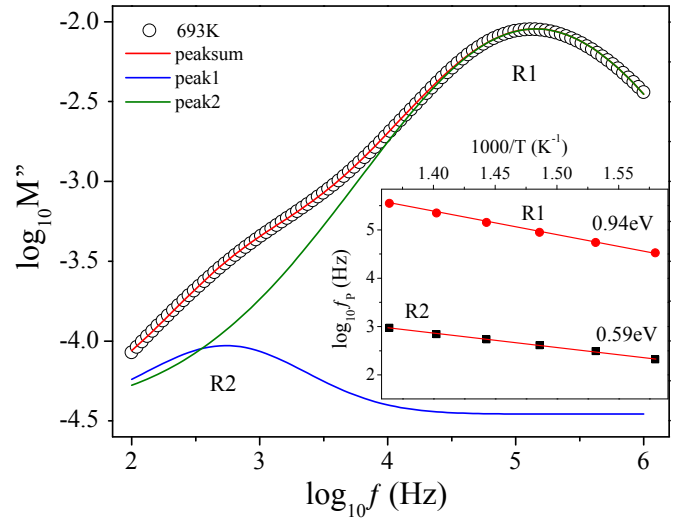


Fig. 5. A typical example showing a comparison between the experimental data (open circles) measured at 693 K and the fitting result (solid lines). The inset shows the Arrhenius plots for R1 and R2 with the data points deduced from the fittings.

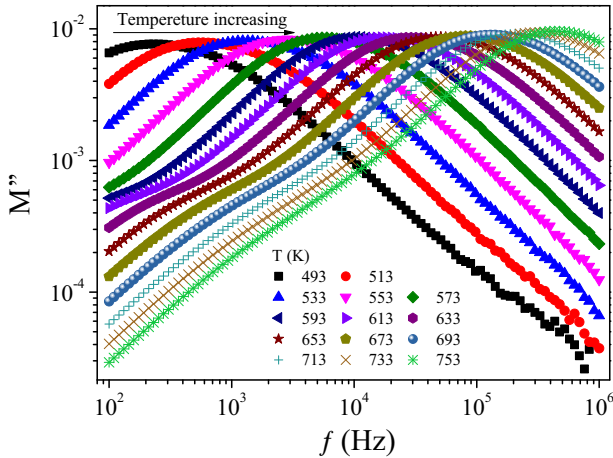


Fig. 4. Frequency dependence of electric modulus at a series of temperatures for a DTO pellet.

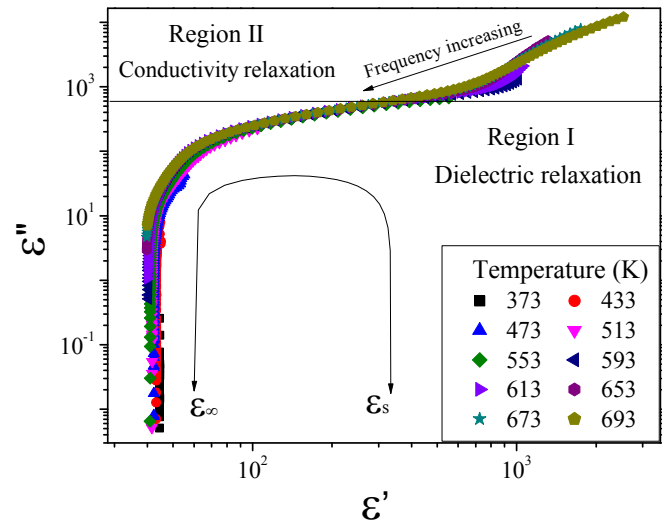


Fig. 6. Cole-Cole plots for DTO at different temperatures.

while the high-frequency terminus tends to the intrinsic dielectric constant (ϵ_{∞}). For the present sample, one notes that the Cole-Cole plots in the high-frequency region (Region I) almost overlap each other, forming a master curve. The high-frequency terminus of each curve points to a constant value (ϵ_{∞}) that decreases with the increasing temperature, confirming the incipient ferroelectric behaviour. Therefore, region I belongs to the high-resistivity dielectric region, and the dielectric properties are dominated by the dielectric relaxation.

However, for the low-frequency region (Region II), instead of tending to ϵ_s , all of the plots exhibit linear tails. When the temperature was elevated higher than ~ 613 K, two linear parts of the tail for each curve can be identified. Our recent work revealed that the oblique tail is a typical feature of a conductivity process [39]. The relaxations in this region are actually conductivity relaxations due to the hopping motions of oxygen vacancies. Therefore, region II is the low-resistivity conductive region, and the dielectric properties are dominated by conductivity relaxation. It is well known that the oxygen vacancies (V_O , also called F or colour centres) are ubiquitous point defects in oxides that are induced by the loss of lattice oxygen (O_O) ions during the high-temperature sintering process, nonstoichiometry, acceptor doping, etc. The ionization of

the oxygen vacancies will create conducting electrons via the equations



where the Kröger-Vink notation of defects is adopted. V_O and V_O^{\cdot} represent singly and doubly ionized oxygen vacancies carrying one and two excess positive charges, respectively. At a high enough temperature, the vacancies become mobile carriers and can contribute to the conductivity in the singly (doubly) charged state in a lower (higher) temperature range. The change of the charge state leads to the two linear parts of the tail found in the Cole-Cole plot. This fact was confirmed by the plot of the ac conductivity, which was obtained in terms of the relationship

$$\sigma(\omega, T) = \omega \epsilon_0 \epsilon''(\omega, T) \quad (5)$$

where ϵ_0 is the electric permittivity of free space. For the sake of clarity, only one ac conductivity curve measured at 1 kHz was plotted in Fig. 7 in terms of the Arrhenius law. The two regions can be well identified: the low-temperature dielectric relaxation (Region I) and the high-temperature conductivity relaxation (Region II). The boundary temperature that separates the two types of relaxation was found to be ~ 435 K, which agrees well with the temperature for the intrinsic dielectric behaviour, as revealed in Fig. 2. The data points in the dielectric relaxation region show large uncertainty due to the sample being an ideal insulator that leads to very small values of conductivity. In the conductive region, two linear Arrhenius segments were found, confirming the two equilibrium states for the conductivity. The presence of the two equilibrium states can be well explained based on the fact that the oxygen vacancies can exist in singly and doubly charged states. It is worth noting that the onset temperatures of the first and second stepwise increases in $\epsilon'(T)$ (Fig. 2(a)) match well with the temperatures where the ac conductivity deviates from the low-temperature equilibrium and tends to the high-temperature equilibrium. Oxygen vacancies that deviate from their original equilibrium state and tend to a new equilibrium state will give rise to a relaxation process [40]. Hence, the low-temperature relaxation (R1) is caused by the deviation of the conductivity from the low-temperature equilibrium state, and the high-temperature relaxation (R2) is due to the trend of the conductivity to the high-temperature equilibrium state [40]. In other words, R1 and R2 can be attributed to the singly and doubly charged oxygen vacancies, respectively. However, it is quite unexpected that the activation energy of R2 is lower than that of R1. The activation energy is related to an energy barrier resulting from the interaction between the relaxing species and its surrounding medium. The higher the charged state of the species, the stronger the interaction, and therefore, the higher the activation energy that is needed to give up the localization of the barrier. Because the relaxing species for R1 and R2 are singly and doubly charged oxygen vacancies, respectively, the activation energy of R2 should be higher than that of R1. This finding suggests a mechanism that facilitates the hopping motion of oxygen vacancies. The mechanism can be well understood based on the fact that the oxygen vacancies in the

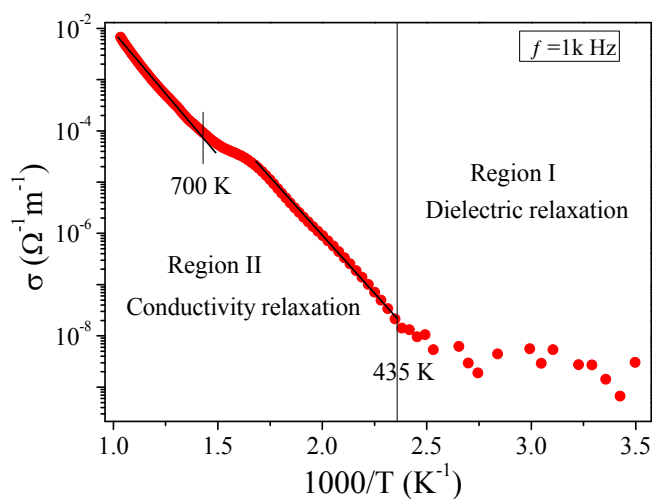


Fig. 7. Arrhenius plot of ac conductivity measured at 1 kHz for a DTO pellet. The straight lines are the linear fitting results, which indicate the two equilibrium conductivity states.

pyrochlore-type structure are ordered, providing fast channels for oxygen diffusion [41]. This is further demonstrated by the high ionic conductivity reported in the pyrochlore-type $\text{Gd}_{2-y}\text{La}_y\text{Zr}_2\text{O}_7$ [42]. The activated energy for the movement of the ordered state is much lower than the summation energy for the movement of individual oxygen vacancies [43].

4. Conclusions

In summary, detailed investigations on the dielectric properties of $\text{Dy}_2\text{Ti}_2\text{O}_7$ ceramics were performed as functions of temperature (4–973 K) and frequency (100 Hz–1 MHz). The sample was confirmed to show incipient ferroelectric behaviour in the temperature range below 450 K, while in the temperature range higher than 450 K, two thermally activated relaxations (R1 and R2) were observed. Both relaxations are related to oxygen vacancies. The mechanisms of R1 and R2 were argued to be a type of conductivity relaxation associated with singly and doubly ionized oxygen vacancies, respectively.

Acknowledgements

The authors acknowledge the financial support from the National Natural Science Foundation of China (Grant Nos. 11404002, 11404003, and 51402001) and the Co-operative Innovation Research Center for Weak Signal-Detecting Materials and Devices Integration of Anhui University (Grant No. 01001795). This work was supported in part by the China Postdoctoral Science Foundation (Grant No. 2014M561805), Anhui Province Postdoctoral Science Foundation (Grant No. 2014B007), and Zhejiang Provincial Natural Science Foundations of China (Grant Nos. LY12F02014 and LY13F010006).

References

- [1] W. Eerenstein, N.D. Mathur, J.F. Scott, *Nature* 442 (2006) 759–765.
- [2] T. Kimura, T. Goto, H. Shintani, K. Ishizaka, T. Arima, Y. Tokura, *Nature* 426 (2003) 55–58.
- [3] T. Goto, T. Kimura, G. Lawes, A.P. Ramirez, Y. Tokura, *Phys. Rev. Lett.* 92 (2004) 257201.
- [4] N. Hur, S. Park, P.A. Sharma, J.S. Ahn, S. Guha, S.-W. Cheong, *Nature* 429 (2004) 392–395.
- [5] I. Burn, S. Neirman, *J. Mater. Sci.* 17 (1982) 3510–3524.
- [6] D.W. Hwang, J.S. Lee, W. Li, S.H. Oh, *J. Phys. Chem. B* 107 (2003) 4963–4970.
- [7] M.A. Subramanian, G. Aravamudan, G.V. Subba Rao, *Prog. Solid State Chem.* 15 (1983) 55–143.
- [8] K.B. Helean, S.V. Ushakov, C.E. Brown, A. Navrotsky, J. Lian, R.C. Ewing, J.M. Farmer, L.A. Boatner, *J. Solid State Chem.* 177 (2004) 1858–1866.
- [9] F.X. Zhang, S.K. Saxena, *Chem. Phys. Lett.* 413 (2005) 248–251.
- [10] N. Zhong, P.-H. Xiang, D.-Z. Sun, X.-L. Dong, *Mater. Sci. Eng. B* 116 (2005) 140–145.
- [11] S.T. Bramwell, M.N. Field, M.J. Harris, I.P. Parkin, *J. Phys. Condens. Matter* 12 (2000) 483–495.
- [12] R. Abe, M. Higashi, K. Sayama, Y. Abe, H. Sugihara, *J. Phys. Chem. B* 110 (2006) 2219–2226.
- [13] H.X. Yan, H.P. Ning, Y.M. Kan, P.L. Wang, M.J. Reece, *J. Am. Ceram. Soc.* 92 (2009) 2270–2275.
- [14] M.J. Harris, M.P. Zinkin, Z. Tun, B.M. Wanklyn, I.P. Swainson, *Phys. Rev. Lett.* 73 (1994) 189–192.
- [15] T. Fennell, P.P. Deen, A.R. Wildes, K. Schmalzl, D. Prabhakaran, A.T. Boothroyd, R.J. Aldus, D.F. McMorrow, S.T. Bramwell, *Science* 326 (2009) 415–417.
- [16] S.T. Bramwell, S.R. Giblin, S. Calder, R.J. Aldus, D. Prabhakaran, T. Fennell, *Nature* 461 (2009) 956–959.
- [17] K.A. Ross, Th Proffen, H.A. Dabkowska, J.A. Quilliam, L.R. Yaraskavitch, J.B. Kycia, B.D. Gaulin, *Phys. Rev. B* 86 (2012) 174424.
- [18] M. Saito, R. Higashinaka, Y. Maeno, *Phys. Rev. B* 72 (2005) 144422.
- [19] M.J. Matthews, C. Castelnovo, R. Moessner, S.A. Grigera, D. Prabhakaran, P. Schiffer, *Phys. Rev. B* 86 (2012) 214419.
- [20] B. Klemke, M. Meissner, P. Strehlow, K. Kiefer, S.A. Grigera, D.A. Tennant, *J. Low. Temp. Phys.* 163 (2011) 345–369.
- [21] D.A. Belov, A.V. Shlyakhtina, S. Yu Stefanovich, A.N. Shchegolikhin, A.V. Knotko, O.K. Karyagina, L.G. Shcherbakova, *Solid State Ion.* 192 (2011) 188–194.
- [22] J.K. Yamamoto, A.S. Bhalla, *Mater. Lett.* 10 (1991) 497–500.

- [23] D. Prabhakaran, A.T. Boothroyd, *J. Cryst. Growth* 318 (2011) 1053–1056.
- [24] K.A. Müller, H. Burkard, *Phys. Rev. B* 19 (1979) 3593–3602.
- [25] I.S. Kim, M. Itoh, T. Nakamura, *J. Solid State Chem.* 101 (1992) 77–86.
- [26] H. Vogt, H. Uwe, *Phys. Rev. B* 29 (1984) 1030–1034.
- [27] L.H. Ni, Y. Niu, C.L. Song, W. Wang, G.R. Han, Y.K. Ge, *Phys. B* 406 (2011) 4145–4149.
- [28] J.H. Barrett, *Phys. Rev.* 86 (1952) 118–120.
- [29] P.H. Sun, T. Nakamura, Y.J. Shan, Y. Inaguma, M. Itoh, *Ferroelectrics* 200 (1997) 93–107.
- [30] H. Liu, Y.M. Zou, S.L. Zhang, R.R. Zhang, C.J. Zhang, Y.H. Zhang, *Rare Met.* 34 (2015) 81–88.
- [31] C.C. Wang, Y.M. Cui, L.W. Zhang, *Appl. Phys. Lett.* 90 (2007) 012904.
- [32] C.C. Wang, J. Wang, X.H. Sun, L.N. Liu, J. Zhang, J. Zheng, C. Cheng, *Solid State Commun.* 179 (2014) 29–33.
- [33] C.C. Wang, H.B. Lu, K.J. Jin, G.Z. Yang, *Mod. Phys. Lett. B* 22 (2008) 1297–1305.
- [34] S.A. Prosdanoyev, N.M. Teslenko, A.V. Fisenko, *J. Phys. Condens. Matter* 5 (1993) 9327–9344.
- [35] B.S. Kang, S.K. Choi, C.H. Park, *J. Appl. Phys.* 94 (2003) 1904–1911.
- [36] P. Moretti, F.M. Michel-Calendini, *Phys. Rev. B* 36 (1987) 3522–3527.
- [37] M.O. Selmer, P. Pecheur, *J. Phys. C. Solid State Phys.* 21 (1988) 1779–1790.
- [38] K.A. Müller, *J. Phys.* 42 (1981) 551–557.
- [39] H.B. Li, C.C. Wang, H. Wang, J. Wang, D. Zhang, N. Zhang, *Ceram. Int.* 41 (2015) 14773–14779.
- [40] C.C. Wang, C.M. Lei, G.J. Wang, X.H. Sun, T. Li, S.G. Huang, H. Wang, Y.D. Li, *J. Appl. Phys.* 113 (2013) 094103.
- [41] M.A. Subramanian, G. Aravamudan, G.V.S. Rao, *Prog. Solid State Chem.* 15 (1983) 55–143.
- [42] J.A. Díaz-Guillén, M.R. Díaz-Guillén, K.P. Padmasree, A.F. Fuentes, J. Santamaría, C. León, *Solid State Ion.* 179 (2008) 2160–2164.
- [43] W. Li, K. Chen, Y.Y. Yao, J.S. Zhu, Y.N. Wang, *Appl. Phys. Lett.* 85 (2004) 4717–4719.